AIAA JOURNAL
Vol. 55, No. 7, July 2017

Wave-Front Measurements of a Supersonic Boundary Layer Using Laser Induced Breakdown

R. Mark Rennie,* Minh Nguyen,† Stanislav Gordeyev,‡ and Eric J. Jumper§
University of Notre Dame, Notre Dame, Indiana 46545
Alan B. Cain¶
Innovative Technology Applications, Chesterfield, Missouri 63006
and
Timothy E. Hayden**
U.S. Air Force Academy, Colorado Springs, Colorado 80840

DOI: 10.2514/1.J055611

The aero-optical effect of a flat-plate adiabatic boundary layer has been measured using the light generated by a laser-induced breakdown spark. The measurements were performed in a blowdown wind tunnel at freestream Mach numbers of 3 and 4.38. The tests showed that the aero-optical effect of boundary layers with rms optical path difference as low as 0.05 μm could be accurately measured using the laser-induced breakdown spark, including their deflection-angle spatial spectra. The results demonstrate that, using the laser-induced breakdown spark as a source of illumination, it is possible to make accurate measurements of low-amplitude aero-optical effects in a manner that is self-contained, nonintrusive, and suitable for a flight-test environment.

Nomenclature

C_f	=	skin friction coefficient
D_L	=	laser lens aperture
d_{AP}	=	measurement aperture diameter
d_L	=	lenslet size
E	=	pulse energy
f_c	=	collimating lens focal length
f_L	=	laser lens focal length
K_{GD}	=	Gladstone–Dale constant
k	=	streamwise wave number
M_∞	=	Mach number
n	=	index of refraction
OPD	=	optical path difference
P_t	=	total pressure
r	=	radial coordinate
St_δ	=	Strouhal number based on δ
t	=	time
U_c	=	disturbance convection velocity
U_∞	=	freestream speed
W	=	wave front
x	=	streamwise coordinate
y	=	cross-stream coordinate
Z_C	=	Zernike coefficient
δ	=	boundary-layer thickness
θ	=	small-aperture deflection angle
$\hat{\theta}$	=	deflection angle spectrum
λ	=	disturbance wavelength
λ_L	=	laser wavelength
ρ	=	density

Received 19 August 2016; revision received 6 January 2017; accepted for publication 10 January 2017; published online 11 April 2017.

*Research Associate Professor, Department of Mechanical and Aerospace Engineering, Hessert Laboratory for Aerospace Research. Senior Member AIAA.

†Graduate Research Assistant, Department of Mechanical and Aerospace Engineering, Hessert Laboratory for Aerospace Research. Student Member AIAA.

‡Associate Professor, Department of Mechanical and Aerospace Engineering, Hessert Laboratory for Aerospace Research. Associate Fellow AIAA.

§Professor, Department of Mechanical and Aerospace Engineering, Hessert Laboratory for Aerospace Research. Fellow AIAA.

¶President. Associate Fellow AIAA.

**Aerospace Engineer, Department of Aeronautics. Senior Member AIAA.

I. Introduction

THE wave front of a beam of light passing through a compressible flow is distorted by spatial and temporal variations of the refractive index within the flow. The refractive-index variations are related to density variations by the Gladstone–Dale relationship:

$$n(\boldsymbol{x}, t) = 1 + K_{\mathrm{GD}}\rho(\boldsymbol{x}, t) \tag{1}$$

where the Gladstone–Dale constant K_{GD} has a value of approximately 2.27×10^{-4} m^3/kg for light at visible and near-infrared wavelengths. The optical distortion on a beam of light transiting the flow is then the average-removed integral of n along the distance traversed by the light beam:

$$\mathrm{OPD}(x, y, t) = \int n'(x, y, z, t)\,\mathrm{d}z \tag{2}$$

where OPD is the optical path difference, prime denotes mean-removed fluctuations, and propagation in the z direction is assumed. The study of the optical effect of compressible flows is called "aero-optics". Examples of recent investigations into the aero-optical effects of boundary layers, shear layers, and shock waves are described in [1–6].

Aero-optical effects are most commonly studied to evaluate their effect on airborne optical systems including directed-energy, imaging, or free-space communications systems. However, because the aberrations are the integrated effect of the flow density field, aero-optical measurements can also be used to extract information on the underlying flow itself. As shown in [1–3], a flight-test measurement of the optical aberration imposed by the (turbulent) vehicle boundary layer can be used to estimate boundary-layer thickness δ, local convection velocity, density, and other boundary-layer parameters; this kind of fluid-mechanic understanding cannot always be obtained from ground-test and computational-fluid-dynamics efforts alone.

Flight-test measurements of the aero-optical effect of a vehicle boundary layer (or other turbulent flow) are complicated by the need for a source of light to provide the interrogating wave front that can be

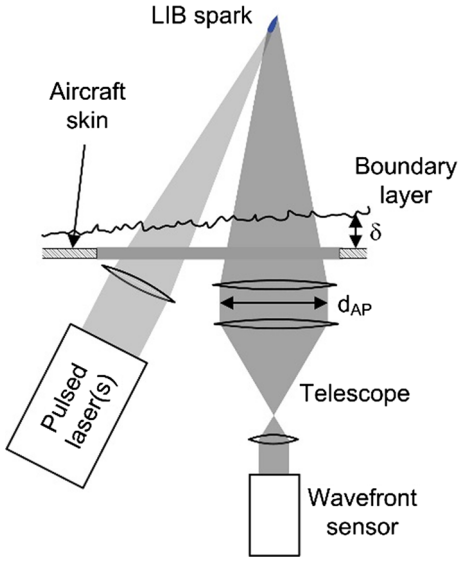

Fig. 1 Basic concept for instrument to measure aero-optical effect of aircraft boundary layer in flight.

reliably generated at different locations in the flow. One approach to solving this problem is to use an artificial light source for aero-optical measurements that is generated by focusing the output of a laser to create a laser-induced breakdown (LIB) spark. In this case, the broadband emission from the LIB is passed through the aero-optical flow of interest and into a wave-front sensor to detect the optical effect of the flow. The advantages of this approach are that the LIB can be formed at any location around the aircraft without the need for mounts or appendages that might perturb the aero-optical flow of interest. A layout of a conceptual instrument to measure the aero-optical effect of the boundary layer on a flight-test vehicle is shown in Fig. 1; such an instrument is both fully self-contained and nonintrusive.

It should be emphasized that the purpose of the LIB in Fig. 1 is to generate a near-point source of light for measurement of the aero-optical flow of interest and not, for example, to investigate the behavior or composition of the LIB itself. In this regard, previous literature on this kind of "aero-optical guide star" is sparse [7–10]. Although "laser guide stars" are commonly used to evaluate atmospheric optical effects on ground-based telescopes [11], these techniques are based on Raleigh scattering or sodium fluorescence and do not involve LIB. In [7], the requirements for LIB measurements of aero-optical flows at hypersonic flow speeds is reviewed, but detailed wave-front data are not shown. In our previous work described in [8–10], the output of a pulsed Nd:YAG laser with wavelength of 355 nm was focused to create an LIB spark, which was successfully used to measure the aero-optical aberrations produced by a compressible shear-layer flow. However, because of the small scale of the wind tunnel used in these investigations, the LIB spark was formed in the quiescent laboratory air outside of the wind tunnel with the generated light directed through the wind-tunnel test section and shear-layer flow; as such, the test did not fully simulate the conditions of an actual flight-test deployment. Furthermore, although the tests showed that the optical aberration of the shear layer could be accurately measured using the technique, the optical effect of the shear layer was quite large so that the tests did not demonstrate the kind of measurement accuracy that can be achieved.

In this paper, the results of an effort to measure the aero-optical effect of a compressible boundary layer using the light from an LIB spark are presented. The measurements were performed at high supersonic Mach numbers and are novel in the sense that the LIB spark was generated in the flow and therefore more faithfully simulates an actual flight-test deployment of the measurement approach. Furthermore, the magnitude of the aero-optical distortion created by the boundary-layer flows under investigation were one to two orders of magnitude less than the shear-layer flows investigated in [8–10], so that the results of these tests represent a more rigorous demonstration of the level of measurement sensitivity that can be achieved using the technique. New methods to remove measurement noise and improve the sensitivity of the technique are also presented.

II. Experiment

The measurements were performed in the Trisonic Wind Tunnel (TWT) at the U.S. Air Force Academy. This tunnel has a blowdown configuration with test-section dimensions of 1×1 ft, maximum Mach number of 4.38, and maximum test-section total pressure of 1.7 MPa. Air storage consists of six 25.5 m^3 tanks that can be pumped to a pressure of 4 MPa, giving up to 7 min of total run time, depending on test conditions. The stored air is first dried to −45°C dew point, filtered, and then heated to around 38°C to prevent water condensation, ice formation, and/or liquefaction in the test section.

The measurements were performed at test-section Mach numbers of $M_\infty = 3.0$ and 4.38. Tunnel conditions for the experiments performed are summarized in Table 1. The flow speeds shown in the table were computed using the storage tank stagnation temperature of 311 K and assuming isentropic flow. The boundary-layer thickness δ and skin friction C_f at the measurement location were estimated from the geometry of the wind-tunnel nozzles using a semi-empirical method described in [12], and δ was also verified by schlieren measurements. The equivalent standard-atmosphere altitude shown in Table 1 is based on the test-section density, which has the most effect on the magnitude of the aero-optical aberration produced by the boundary layer and hence signal strength of the measurements.

A. Laser-Induced Breakdown Measurements

A schematic and photograph showing the optical setup for the LIB spark measurements in the TWT test section are shown in Fig. 2. The experiments were performed with an empty test section. An LIB spark was formed near the far wall of the test section by focusing the output of an Nd:YAG pulsed laser with wavelength $\lambda_L = 355$ nm and pulse duration $\Delta t = 5$ ns through a fused-silica window with good UV transmission properties. The advantage of the 355 nm wavelength is that, because the focal region of the focused laser beam becomes smaller as the wavelength is reduced, breakdown can be achieved with less pulse energy so that smaller LIB sparks can be formed, thereby improving the performance of the wave-front measurements [8–10].

The laser beam was first expanded to a diameter of 50 mm and focused using a 500 mm focal length lens, giving an f number for the focused beam of $f_L/D_L = 10$. Beam pulse energies E just above the breakdown threshold were used to generate the LIB spark and are shown in Table 1. The mean irradiance at the beam focal point,

Table 1 Summary of test conditions for LIB spark measurements

Parameter	Test 1	Test 2	Test 3	Test 4	Test 5
Mach number	4.38	3.0	3.0	3.0	3.0
Total pressure, MPa	1.5	1.4	1.0	0.7	0.5
Density, kg/m^3	0.36	1.13	0.86	0.57	0.42
Flow speed, m/s	704 ± 2	633 ± 2	633 ± 2	633 ± 2	633 ± 2
δ, mm	26 ± 2.5	16 ± 1.5	16 ± 1.5	16 ± 1.5	16 ± 1.5
Equivalent altitude, km	11.1	0.8	3.5	7.3	9.7
Laser pulse energy, mJ	$18–25 \pm 2.6$	10.6 ± 2.6	11.8 ± 2.6	12.6 ± 2.6	15.8 ± 2.6

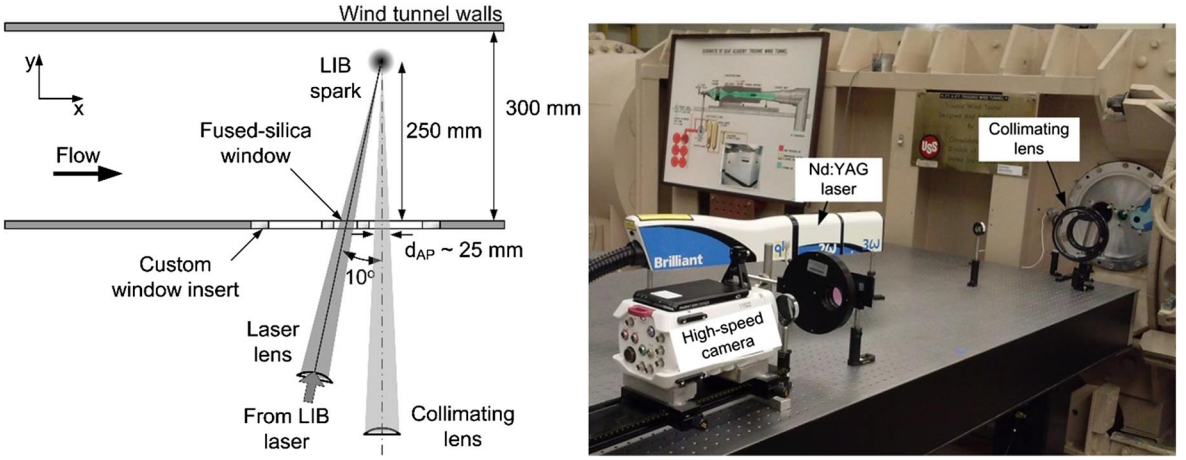

Fig. 2 Schematic (left) and photograph (right) of experiment to measure aero-optical effect of wall boundary layer of the Trisonic Wind Tunnel using return light from an LIB spark.

computed using Eq. (3) [13], was in the range 1.5 to 3×10^{13} W/cm^2; these irradiances are comparable to breakdown thresholds reported in, for example, [14]. No flow seeding or other measures were taken to aid the generation of LIB:

$$I = \frac{E}{4\pi\Delta t[(\lambda_L f_L)/\pi D_L]^2} \tag{3}$$

After passing through the wall boundary layer of the TWT test section, the light from the LIB spark was collected using a collimating lens (see Fig. 2), passed through a beam reducer, and into a wave-front sensor. The wave-front sensor consisted of a lenslet array with 38.1 mm focal length and 0.3 mm lenslet pitch attached to a high-speed camera. The beam size on the charge-coupled device (CCD) sensor was typically sized to span around 50 lenslets, with pixel resolution of ~15 pixels per lenslet. The sampling frequency of the measurements was 10 Hz, which was dictated by the pulse repetition rate of the Nd:YAG laser. The exposure time of the wave-front sensor camera was also much longer than the 5 ns pulse duration of the laser, so that the wave-front sensor captured the full emission of the LIB spark. With this setup, the brightness of the LIB spark generated with the pulse energies shown in Table 1 was found to be sufficient for good wave-front measurements.

B. Continuous-Wave Laser Measurements

Wave-front measurements of the TWT boundary layer were also made using a collimated, continuous-wave (CW) laser beam and used to compare with the data obtained using the LIB spark. A schematic showing the setup for the experiments using the CW laser is shown in Fig. 3. For these tests, a collimated 25-mm-diam, 532-nm-wavelength light beam was directed through the empty test section normal to the optical-access windows. A return mirror on the other side of the test section was used to reflect the beam back through the test section and into a wave-front sensor, so that the beam passed through both wall boundary layers twice, amplifying the optical aberration detected by the CW beam by a factor of $2\sqrt{2}$ [1]. The wave-front sensor had the same configuration as the LIB tests, that is, a high-speed camera with a 38.1 mm focal length lenslet array with 0.3 mm lenslet pitch. CW measurements of the boundary-layer aero-optical effect were performed at test-section conditions corresponding to tests 1 and 3 of Table 1 ($M_\infty = 3.0$, $P_t = 1.0$ MPa and $M_\infty = 4.38$, $P_t = 1.5$ MPa). Additional information on the CW measurements can be found in [15].

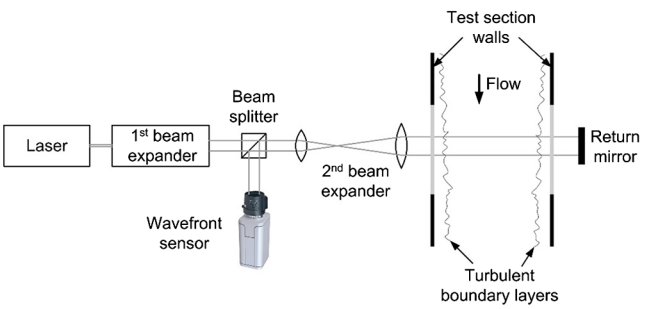

Fig. 3 Schematic of experiment to measure aero-optical effect of TWT wall boundary-layers using CW laser.

III. Results

Figure 4 shows an example of a single unprocessed image from the wave-front sensor acquired using the LIB spark. Each "dot" in the unprocessed image is formed by a lenslet in the lenslet array and is an image of the LIB spark itself on the wave-front sensor camera CCD array. Close inspection of Fig. 4 shows that the individual spark images become more elongated toward the edges of the measurement aperture. This elongation is the result of the different aspect of the LIB spark as "viewed" by the individual lenslets in the lenslet array, so that the spark appears elongated in the perspective of the lenslets located on the edge of the aperture. Previous work on how the wave-front measurements are affected by the size and shape of the LIB spark can be found in [10].

The gray regions at the top and bottom of Fig. 4 are regions of the camera CCD array that were outside of the extent of the lenslet array. These regions were removed by applying a circular aperture with diameter $d_{AP} = 25$ mm to the dot pattern; see Fig. 4. Wave fronts were then computed from the apertured dot patterns using standard methods. Specifically, "areas of interest" (AOIs) were defined around each dot (i.e., spark image) in the raw camera images, after which dot locations were determined using a first-order centroiding algorithm [16]. Reference locations for the dots were then computed as the average over all images for a given test, and wave-front slopes were computed based on the dot deflections from their reference locations. Wave fronts were reconstructed from the wave-front slopes using the Southwell method [17], and optical tip, tilt, and piston were removed from the wave fronts using a least-squares plane-fitting calculation. Figure 4, right, shows a typical wave front computed using this methodology.

A. Compensation for Spark Motion Effect

A consequence of using the LIB spark for wave-front measurements is that the resulting wave fronts can be altered by the effect of motions of the LIB spark itself. As shown in [10], these motion-induced variations of the LIB spark wave front are produced even in still air, where in this case the spark motions are produced by small displacements in the exact location of the LIB spark and/or variations in the shape of the spark between spark ignitions. Because the wave front for an individual measurement is computed from the displacements of the raw dot locations from the reference dot

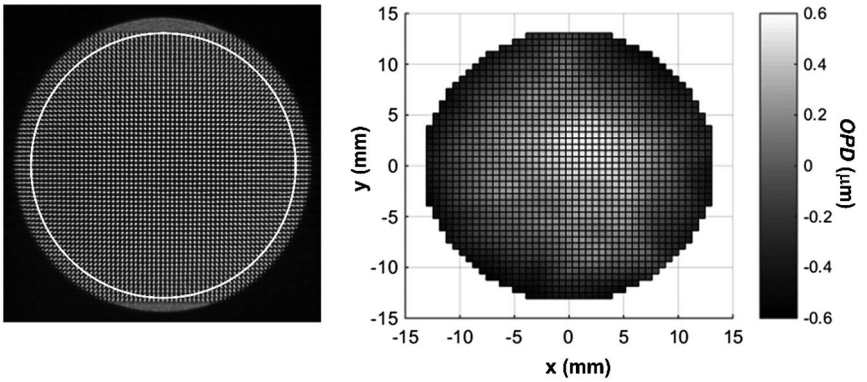

Fig. 4 Typical unprocessed dot pattern (left) from wave-front sensor with circular aperture shown, and sample wave front (right) computed from apertured dot pattern.

locations (that were ensemble-averaged over multiple measurements; see Fig. 4 and preceding explanation), small variations in the spark shape or effective location for an individual measurement can alter the dot pattern and resulting wave front in a manner that is unrelated to the aero-optical effect of the flow under test.

A distinction between the current study and the previous results reported in [10] is that spark motion could also have been produced by convection of the spark with the tunnel flow, which moved at a speed of up to 704 m/s in a direction perpendicular to the line of sight of the wave-front measurements; see Table 1 and Fig. 2. As shown in [18], if laser pulse energies significantly greater than the breakdown threshold are used, the spark can have a lifetime (i.e., the time duration over which the spark emission is detectable by the wave-front sensor camera) that is significantly longer than the laser pulse duration and on the order of several microseconds. However, for the LIB wave-front measurements described here, the laser pulse energy was reduced to the minimum level that produced raw dot patterns that were just bright enough for accurate measurements; as such, the effective spark lifetime was likely much shorter and on the order of 1 μs or less. More importantly, it is worth repeating that it is the spark-to-spark variation of the spark convected motion from the mean that produces the motion-induced LIB aberration, which is much less than the absolute convected motion. Finally, as shown by the optical setup in Fig. 2, the convected motion of the spark was perpendicular to the wave-front sensor line of sight so that the LIB convected motion would be expected to produce primarily optical tip/tilt, which was not used in the current study and was removed from the data (given previously). In summary, although no attempt was made to evaluate it in detail, it is possible that the convected motion of the LIB spark could also have had an effect on the wave-front results, but this effect was likely much smaller than the variations in spark location that occur even in still air and are reported in [10].

In [10], it was shown that the motion-related wave-front distortions of the spark emitted light are primarily characterized by the Zernike defocus mode [19] with a small amount of comatic aberration also present. Figure 5 [10] illustrates how Zernike defocus arises from small displacements ε of the spark toward or away from the focal point of the lens used to collimate the spark emitted light; referring to Fig. 4, it is seen that the sample LIB wave front clearly shows a significant defocus component. Note that aberrations including defocus, coma, etc., could also conceivably have been added to the measured wave fronts by imperfections in the optical setup used to collect and direct the spark light into the wave-front sensor; however, again these aberrations are nonvariant from measurement to measurement and are effectively "zeroed out" when the reference dot locations are computed via the averaging of multiple measurements.

Based on the findings of [10], a Zernike decomposition of the wave fronts measured using the LIB spark was performed. The result for a typical data set is plotted in Fig. 6, which shows the magnitudes of the first 40 Zernike coefficients for wave fronts acquired at $M_\infty = 3$, $P_t = 1.0$ MPa. In Fig. 6, the magnitude of the Zernike coefficient for each mode represents the contribution of that mode to the overall rms of the spatial wave-front distortion $\mathrm{OPD}_{\mathrm{rms}}$. Included in the figure is an equivalent Zernike decomposition of a set of wave fronts acquired using the CW laser at the same Mach number and using the same size of measurement aperture. Figure 6 clearly shows that the spark wave fronts are affected primarily by defocus (Zernike mode 4) and some coma (mode 7) in agreement with [10]. The results in Fig. 6 extend upon the findings of [10] by showing that the LIB also produces some astigmatism (mode 6) and by quantifying the magnitude of the LIB

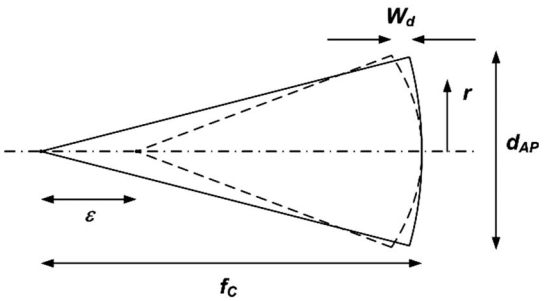

Fig. 5 Schematic showing how small displacements ε of the LIB spark toward or away from the collimating lens produce residual defocus on the measured wave front [10].

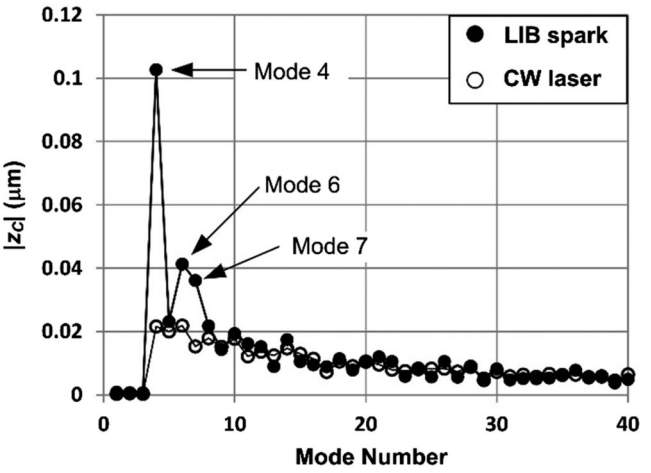

Fig. 6 Zernike coefficient magnitudes for a data set acquired at $M_\infty = 3$, $P_t = 1.0$ MPa.

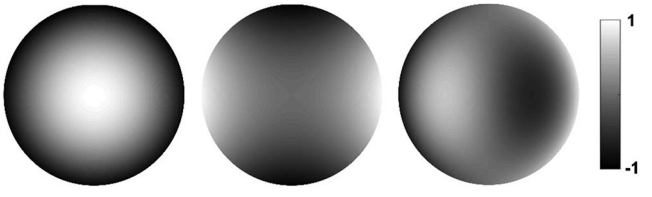

Fig. 7 Nondimensional Zernike modes 4, 6, and 7.

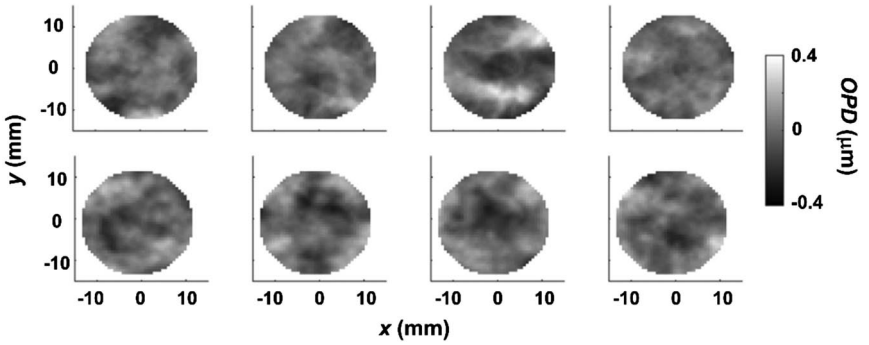

Fig. 8 Examples of wave fronts acquired using LIB spark with Zernike modes 4, 6, and 7 removed (top row) and using CW illumination (bottom row), $M_\infty = 3$, $P_t = 1.4$ MPa, $\delta = 15$ mm, $d_{AP} = 25$ mm.

effect via comparison with equivalent CW data. Diagrams of the Zernike defocus, astigmatism, and coma modes are shown in Fig. 7 for reference.

In [10], it is shown that the OPD_{rms} contributed by the Zernike defocus mode (Z_{C4}) can be related to spark motion ε by

$$Z_{C4} = \frac{\varepsilon}{27.7[f_C/D_C]^2} \tag{4}$$

In Eq. (4), f_C/D_C is the f number of the collimating lens used to collect the light from the LIB spark, where $f_C/D_C = 10$ for the LIB wave-front measurements as shown in Fig. 2. Using the result $Z_{C4} \sim 0.1\ \mu$m from Fig. 6 gives $\varepsilon \sim 0.27$ mm. This result corresponds reasonably well with typical variations of spark dimensions reported in [10] and other studies.

In general, wave-front distortions produced by compressible boundary layers and other aero-optical flows are very poorly represented by Zernike modes, as demonstrated by the slow convergence of the Zernike coefficients for the CW wave fronts shown in Fig. 6. This is because the radial and azimuthal symmetries of the Zernike mode shapes fail to capture the dominant streamwise orientation of boundary-layer aero-optical disturbances. As such, a first approach to removing the effect of LIB spark motion is to simply subtract the affected Zernike modes from the measured wave fronts. The top row of Fig. 8 shows a sample of four wave fronts acquired using the LIB spark with Zernike modes 4, 6, and 7 removed. The wave fronts in Fig. 8 no longer show the strong defocus mode present in Fig. 4 (right) and are much more representative of boundary-layer aero-optical disturbances; specifically, they show dominant optical-structure sizes on the order of the boundary-layer thickness in agreement with boundary-layer aero-optical behavior described in [1–4]. Four wave fronts acquired using CW illumination are also shown in the bottom row of Fig. 8 and show qualitatively similar characteristics and structure sizes to the aforementioned LIB wave fronts.

In [1,2], the OPD_{rms} of the aero-optical aberrations produced by a flat-plate adiabatic boundary layer was modeled using

$$OPD_{rms} = K_{GD}\rho_\infty M_\infty^2 \delta \sqrt{C_f} F(M_\infty) \tag{5}$$

where $F(M_\infty)$ is an empirical function shown in Fig. 9. In [3], a model for the boundary layer was developed that had similar functional form to Eq. (5) but with slightly different $F(M_\infty)$ that is also shown in Fig. 9. The OPD_{rms} that was computed for the full-aperture, CW measurements made at $M_\infty = 3$ and 4.38 were shown to match the models within experimental error; see data points in Fig. 9 [15]. As shown in Table 1, tests 2 to 5 were performed at $M_\infty = 3$ but at different total pressures and hence static densities; a plot of the OPD_{rms} for the data acquired using the LIB spark for these tests, and with Zernike modes 4, 6, and 7 removed, is shown in Fig. 10. The figure includes Eq. (5) and shows that the LIB results also match the model within experimental uncertainty. Figures 8 and 10 therefore demonstrate that, after correcting for the Zernike modes imposed by the LIB itself, it is possible to make accurate

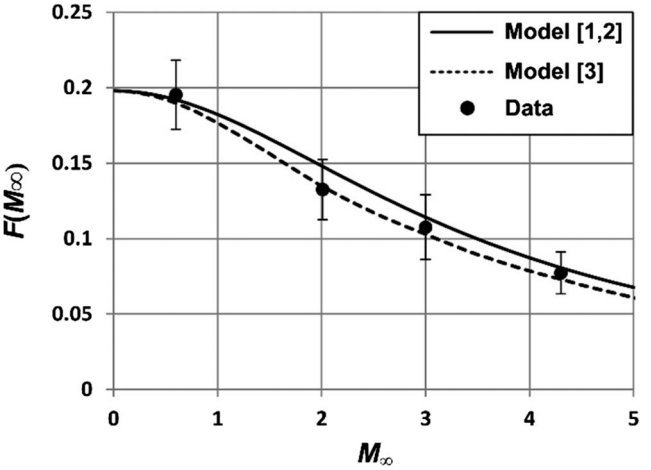

Fig. 9 Empirical function $F(M_\infty)$ for OPD_{rms} of aero-optical effect of flat-plate, adiabatic boundary layer [1–3,15].

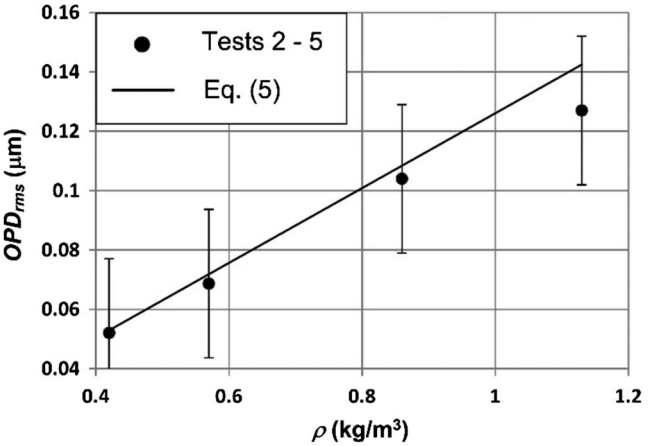

Fig. 10 Spatial OPD_{rms} for tests 2 to 5 in Table 1, with Zernike modes 4, 6, and 7 removed.

measurements of boundary-layer optical distortions and OPD_{rms} using the LIB spark at altitudes up to at least the maximum shown in Table 1, where the local air density and hence strength of the optical signal is significantly reduced.

B. Deflection-Angle Spatial Spectra

The deflection-angle temporal spectrum is typically calculated from measurements of the motion of one or more small-aperture light beams acquired at sufficiently high sampling rate to resolve the spectral content of the boundary-layer aero-optical effect. However, because the sampling rate of the LIB measurements was limited to 10 Hz by the pulse-repetition rate of the LIB laser, deflection-angle

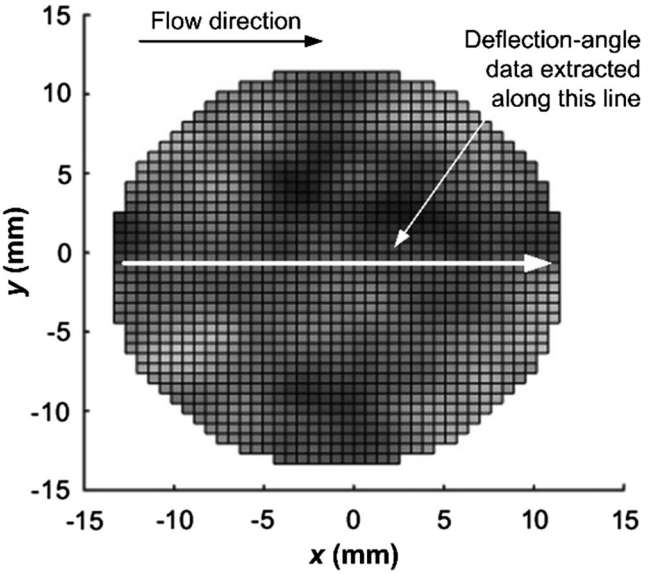

Fig. 11 Diagram illustrating extraction of deflection-angle data from centerline of individual wave fronts.

data for the LIB tests were instead estimated from the slope of the wave-front data $\mathrm{d}W/\mathrm{d}x$ calculated along the centerline of individual wave-front snapshots in the streamwise direction (after removal of Zernike modes 4, 6, and 7), as depicted in Fig. 11:

$$\theta(x) = \frac{\mathrm{d}W(x)}{\mathrm{d}x} \tag{6}$$

Deflection-angle (also referred as jitter) spatial spectral densities, $|\hat{\theta}(k)|^2$, shown in in Figs. 12–15, are plotted against the ratio $\delta k/2\pi = \delta/\lambda$, where λ is the wavelength, and k is the wave number of the aero-optical disturbance. Note that, for small-aperture measurements made at high sampling rate, the deflection-angle temporal spectra are instead normally plotted against the Strouhal number based on the sampling frequency St_δ [1–3,15]; however, the two methods yield essentially the same results with the same spectral behavior and are simply related by the convection speed U_c of aero-optical structures, $\omega = 2\pi f = U_c k$ [1]. From here, it is straightforward to show that the normalized streamwise wave number $\delta k/2\pi$ is related to the Strouhal number based on δ, as $\delta k/(2\pi) = f\delta/U_c = U_\infty/U_c St_\delta$. The ratio U_c/U_∞ is a weak function of the Mach number [15,20]. For a flat-plate adiabatic boundary layer, $U_c \sim 0.88U_\infty$ for $M_\infty = 3$, increasing to $0.9U_\infty$ for $M_\infty = 4.38$ [3,15]. As shown in [20], $\hat{\theta}$ has characteristics that are similar for equilibrium flat-plate boundary-layer flows over a wide range of Mach numbers; specifically, the peak of the spectrum occurs at $St_\delta \sim 1$ or, in wave-number space, at $\delta k/(2\pi) \sim 1.1$. Thus, the peak location in the spectrum can be used to estimate δ. Overall aero-optical distortions can subsequently be computed from the spatial spectrum:

$$\mathrm{OPD}_{\mathrm{rms}}^2 = \frac{1}{\pi}\int_0^\infty |\hat{\theta}(k)|^2 \,\mathrm{d}k$$

Deflection-angle spectral densities computed from the LIB data and the CW data are compared in Fig. 12 for $M_\infty = 3$ and in Fig. 13 for $M_\infty = 4.38$. The LIB data in the figures show the ensemble average of 100–150 separate jitter measurements, with the error bars showing the uncertainty at the 95% confidence level. Note that the maximum wave number resolvable by the method is related to the lenslet size in the wave-front sensor lenslet array giving

$$\left(\frac{\delta k}{2\pi}\right)_{\mathrm{MAX}} = \frac{\delta}{d_L} \tag{7}$$

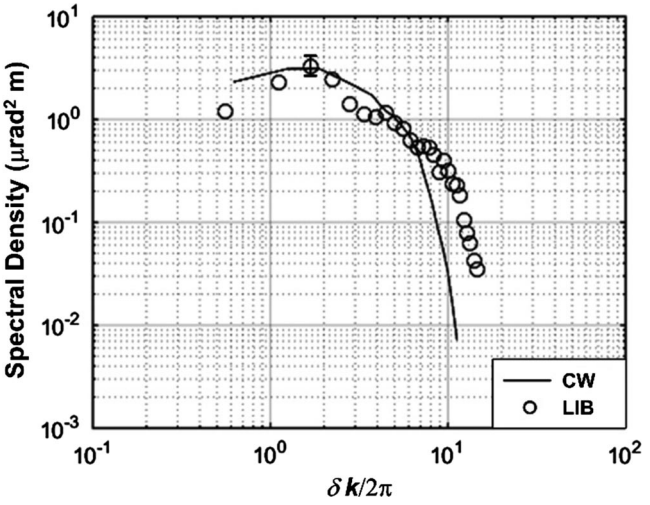

Fig. 12 Deflection-angle spectral densities measured using LIB (with Zernike modes 4, 6, and 7 removed) and CW illumination, $M_\infty = 3$, $P_t = 1.0$ MPa, $d_{\mathrm{AP}} = 25$ mm.

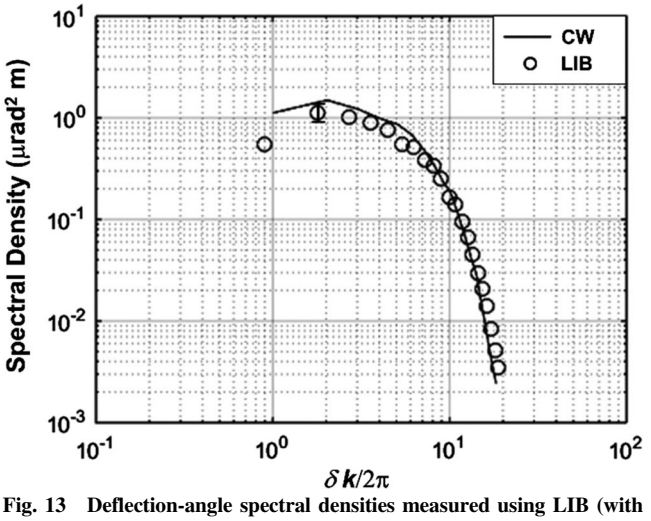

Fig. 13 Deflection-angle spectral densities measured using LIB (with Zernike modes 4, 6, and 7 removed) and CW illumination, $M_\infty = 4.38$, $P_t = 1.5$ MPa, $d_{\mathrm{AP}} = 25$ mm.

Similarly, the minimum resolvable wave number is

$$\left(\frac{\delta k}{2\pi}\right)_{\mathrm{MIN}} = \frac{\delta}{d_{\mathrm{AP}}} \tag{8}$$

The jitter spectra for all tests performed at $M_\infty = 3$ (tests 2 to 5 in Table 1) are summarized in Fig. 14, which shows how the jitter spectrum shifts due to changes in $\mathrm{OPD}_{\mathrm{rms}}$ caused by different ρ_∞.

Figures 12 and 13 show that the spectral densities computed from the individual LIB wave fronts, after removal of Zernike modes 4, 6, and 7, are generally within experimental uncertainty of the spectra calculated from the CW data. The divergence between the LIB and CW spectra at large wave numbers visible in Fig. 12 is most likely caused by the lower signal-to-noise ratio of the LIB measurements, which only sampled the wall boundary-layer once and therefore did not have the $2\sqrt{2}$ signal amplification of the CW beam (from passing through the test section twice; see Sec. II). More importantly, Figs. 12 and 13 also show a discrepancy between the LIB and CW spectra at the lowest wave numbers, especially at $M_\infty = 3$ (Fig. 12), where the LIB spectra generally show smaller amplitudes than the CW spectra. This discrepancy can be attributed to the removal of the low-order Zernike modes performed to compensate for the effects of LIB spark motion. Figure 16 shows curves extracted along the centerline of the

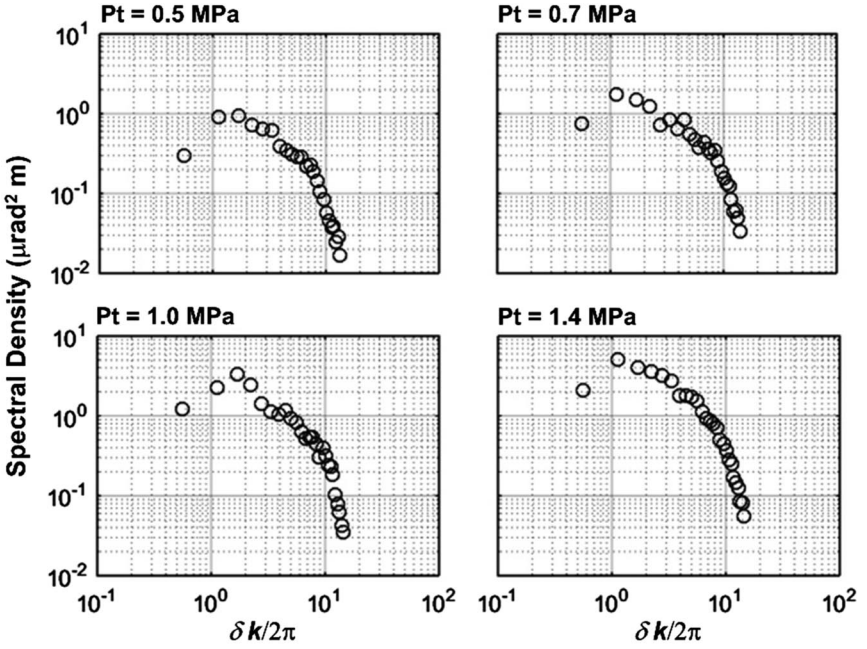

Fig. 14 Deflection-angle spectral densities measured using LIB (with Zernike modes 4, 6, and 7 removed) for tests 2 to 5 in Table 1.

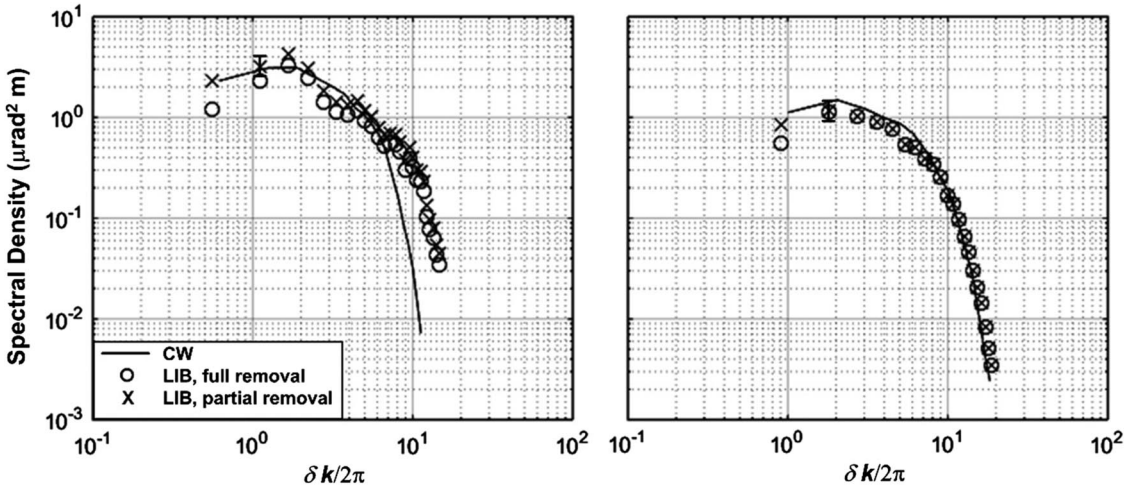

Fig. 15 Deflection-angle spectral densities with full and partial removal of Zernike modes 4, 6, 7 using method of Fig. 17, for tests 3 (left) and 1 (right) of Table 1.

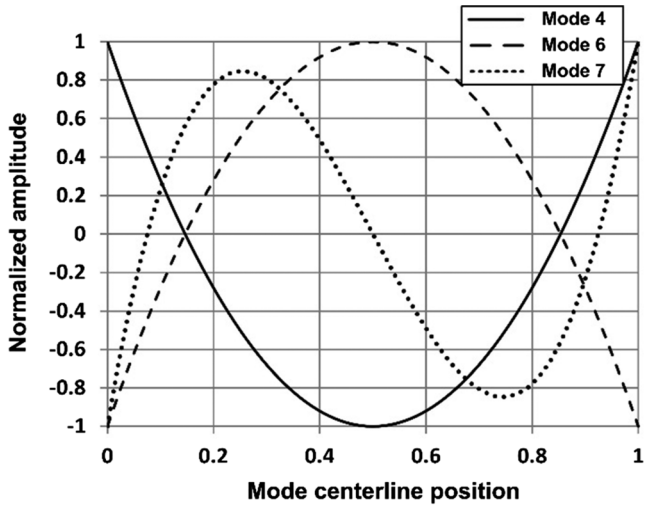

Fig. 16 Normalized plots along centerline of Zernike modes 4, 6, and 7.

Zernike modes 4, 6, and 7 and clearly illustrates the low-frequency sinusoidal appearance of the modes, so that complete removal of the Zernike modes 4, 6, and 7 from the LIB data may also remove low-frequency components of the actual boundary-layer aero-optical effect. As mentioned previously, the peak of the spectrum occurs at $\delta k/(2\pi) \sim 1.1$. This means that, in situations where the measurements are performed on an unknown flow in a flight-test environment, the inability to accurately resolve the low-wave-number components of $\hat{\theta}$ using the LIB spark could compromise the ability to accurately determine the boundary-layer aero-optical effect, especially if the lowest-wave-number component(s) of $\hat{\theta}$ occur in the range $\delta k/(2\pi) \sim 1$.

The fact that the LIB spectrum in Fig. 13 matches the CW data better than in Fig. 12 was most likely the result of a more-optimum adjustment of the laser pulse energy to produce a smaller LIB spark that had less variation from spark to spark yet was still bright enough for good wave-front measurements. As such, one method of achieving better $\hat{\theta}$ spectra would be to fine tune the laser pulse energy for each test; however, this may not be easily achievable and, in any case, would still not eliminate all of the LIB aberrations. Referring to

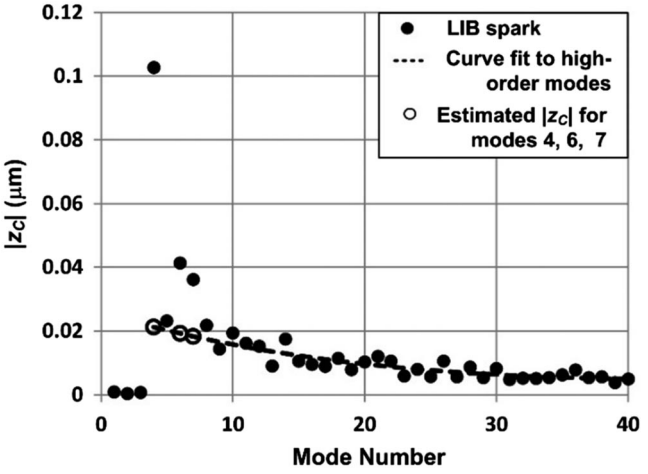

Fig. 17 Method for improved estimate of $|z_C|$ for modes 4, 6, and 7.

Eq. (8), another method of improving the accuracy of the jitter spectrum in the range $\delta k/(2\pi) \sim 1$ would be to use a large measurement aperture d_{AP} which would decrease the ratio δ/d_{AP} and hence shift the Zernike-affected range of the spectrum to lower wave numbers. However, this option may be impractical for large δ and/or flight-test measurements where space is limited.

An alternative and preferable approach to better resolving the low-wave-number components of $\hat{\theta}$ is to attempt to remove only the part of the Zernike modes 4, 6, and 7 that are actually affected by the spark motion. Referring to Fig. 6, it is clear from the CW data that the boundary-layer aero-optical effect contains nonzero magnitudes of the Zernike modes 4, 6, and 7, so that full removal of these modes also removes part of the actual boundary-layer aero-optical signal. In an effort to more accurately account for the effect of the LIB motion, these modes were instead reduced to the levels that would exist normally, that is, the levels measured using the CW illumination. Because the Zernike-mode amplitudes for the LIB and CW data closely match at high mode numbers, this improved estimate of the jitter energy at the lowest St_δ was obtained by extrapolating backward from the high-order LIB Zernike coefficients to estimate the values of modes 4, 6, and 7 that would exist in the absence of spark motions. The result of this method of estimating the coefficient magnitudes for modes 4, 6, and 7 is illustrated in Fig. 17, where the curve fit to the higher-order modes was produced by a simple polynomial (in this case, cubic) fit to modes 9 through 40. Note that this method does not predict the sign of the estimated Zernike coefficients 4, 6, and 7; rather, the sign of these modes from the decomposition of the original, raw wave fronts was maintained, and only the magnitude of the Zernike modes 4, 6, and 7 was estimated. Despite this limitation, Fig. 15 shows that the method produces an improved approximation of the jitter energy at the lowest frequency of the $\hat{\theta}$ spectrum that more closely matches the CW data.

IV. Conclusions

The investigation has demonstrated that it is possible to accurately measure the aero-optical effects of flat-plate boundary-layer flows, including $\mathrm{OPD}_{\mathrm{rms}}$ and deflection-angle spatial spectra, using the light emitted by an laser-induced breakdown (LIB) spark. A key step in the measurement technique is the handling of wave-front distortions caused by motion of the LIB spark itself. The investigation has shown that these wave-front distortions can be identified via a Zernike analysis and removed by subtraction of a few low-order Zernike modes, specifically defocus, coma, and astigmatism. Other important contributions of the investigation include the complete identification of all Zernike modes affected by the LIB motion and evaluation of their typical magnitudes by comparison with equivalent continuous-wave data acquired for the same flow and measurement aperture; these kinds of results have not appeared previously in the literature.

As such, the investigation has shown that, after correction for the LIB-induced Zernike modes, it is possible to measure very low optical signals using the LIB spark. Specifically, boundary-layer wave fronts with $\mathrm{OPD}_{\mathrm{rms}}$ as low as 0.053 μm were successfully measured using the LIB emission, corresponding to the expected aero-optical signal of a flat-plate turbulent boundary layer with $\delta = 16$ mm at an altitude of 9700 m. This is especially significant if it is recognized that the measurements were made with only a single pass of the interrogating LIB light through the boundary-layer flow, in a manner that reproduces the kind of measurement that would be made in an actual flight-test situation. Furthermore, the measurements were performed with the LIB spark formed in the flow, with no observed effect of the flow on the wave-front measurements.

Future efforts should continue to be directed toward methods of mitigating the effect of spark motion or eliminating it altogether. For example, there is likely a preferred orientation of the spark with respect to the measurement aperture that minimizes the influence of the spark motion effects on the measured aero-optical data.

Acknowledgments

This work has been supported by the U.S. Air Force Office of Scientific Research (AFOSR) contract number FA9550-13-C-0010. The U.S. Government is authorized to reproduce and distribute reprints for governmental purposes notwithstanding any copyright notation thereon. Any opinions, findings and conclusions or recommendations expressed in this material are those of the authors and do not necessarily reflect the views of the AFOSR.

References

[1] Gordeyev, S., Smith, A. E., Cress, J. A., and Jumper, E. J., "Experimental Studies of Aero-Optical Properties of Subsonic Turbulent Boundary Layers," *Journal of Fluid Mechanics*, Vol. 740, Jan. 2014, pp. 214–253. doi:10.1017/jfm.2013.658

[2] Gordeyev, S., Jumper, E. J., and Hayden, T. E., "Aero-Optical Effects of Supersonic Boundary Layers," *AIAA Journal*, Vol. 50, No. 3, 2012, pp. 682–690. doi:10.2514/1.J051266

[3] Wyckham, C. M., and Smits, A. J., "Aero-Optic Distortion in Transonic and Hypersonic Turbulent Boundary Layers," *AIAA Journal*, Vol. 47, No. 9, 2009, pp. 2158–2168. doi:10.2514/1.41453

[4] Gordeyev, S., Smith, A. E., Cress, J. A., and Jumper, E. J., "Aero-Optical Measurements in a Subsonic, Turbulent Boundary Layer with Non-Adiabatic Walls," *Physics of Fluids*, Vol. 27, No. 4, 2015, Paper 045110. doi:10.1063/1.4919331

[5] Rennie, R. M., Duffin, D. A., and Jumper, E. J., "Characterization and Aero-Optic Correction of a Forced Two-Dimensional, Weakly-Compressible Shear Layer," *AIAA Journal*, Vol. 46, No. 11, 2008, pp. 2787–2795. doi:10.2514/1.35290

[6] Vorobiev, A., Gordeyev, S., Jumper, E. J., Gogineni, S., Marruffo, A., and Wittich, D. J., "Low-Dimensional Dynamics and Modeling of Shock-Separation Interaction over Turrets at Transonic Speeds," *45th AIAA Plasmadynamics and Lasers Conference*, AIAA Paper 2014-2357, June 2014.

[7] Neal, D. R., Armstrong, D. J., Hedlund, E., Lederer, M., Collier, A., Spring, C., Gruetzner, J., Hebner, G., and Mansell, J., "Wavefront Sensor Testing in Hypersonic Flows Using a Laser-Spark Guide Star," *SPIE Proceedings*, Vol. 3172, July 1997, pp. 349–361.

[8] Rennie, R. M., Whiteley, M. R., Cross, G., Cavalieri, D., and Jumper, E. J., "Optical Measurements of a Compressible Shear Layer Using a Laser-Induced Air Breakdown Beacon," *48th AIAA Aerospace Sciences Meeting*, AIAA Paper 2010-1158, Jan. 2010.

[9] Rennie, R. M., Goorskey, D., Whiteley, M. R., Cavalieri, D., and Jumper, E. J., "Evaluation of Laser Beacon for Adaptive-Optic Correction of a Compressible Shear Layer," *AIAA Journal*, Vol. 51, No. 4, 2013, pp. 1008–1011. doi:10.2514/1.J052254

[10] Rennie, R. M., Goorskey, D., Whiteley, M. R., and Jumper, E. J., "Wavefront Measurements of a Laser-Induced Breakdown Spark in Still Air," *Applied Optics*, Vol. 51, No. 11, 2012, pp. 2306–2314.

[11] Rigaut, F., and Gendron, E., "Laser Guide Star in Adaptive Optics—The Tilt Determination Problem," *Astronomy and Astrophysics*, Vol. 261, No. 2, 1992, pp. 677–684.

[12] Stratford, B. S., and Beaver, G. S., "The Calculation of the Compressible Turbulent Boundary Layer in an Arbitrary Pressure Gradient—A Correlation of Certain Previous Methods," Ministry of Aviation, Aeronautical Research Council, Reports and Memoranda 3207, London, 1961.

[13] Svelto, O., *Principles of Lasers*, 4th ed., Plenum Press, New York, 1998, pp. 148–154.

[14] Tambay, R., Muthu, D. V. S., Kumar, V., and Thareja, R. K., "Laser Induced Breakdown Using 0.355, 0.532, and 1.06 μm Radiation," *Pramana Journal of Physics*, Vol. 37, No. 2, 1991, pp. 163–166. doi:10.1007/BF02875303

[15] Gordeyev, S., Rennie, R. M., Cain, A. B., and Hayden, T. E., "Aero-Optical Measurements of High-Mach Supersonic Boundary Layers," *46th AIAA Plasmadynamics and Lasers Conference*, AIAA Paper 2015-3246, June 2015.

[16] Nightingale, A. M., and Gordeyev, S., "Shack-Hartmann Wavefront Sensor Image Analysis: A Comparison of Centroiding Methods and Image Processing Techniques," *Journal of Optical Engineering*, Vol. 52, No. 7, 2013, Paper 071413. doi:10.1117/1.OE.52.7.071413

[17] Southwell, W. H., "Wave-Front Estimation from Wave-Front Slope Measurements," *Journal of the Optical Society of America*, Vol. 70, No. 8, 1980, pp. 998–1006. doi:10.1364/JOSA.70.000998

[18] Rennie, R. M., Nguyen, M., Gordeyev, S., Cain, A. B., and Hayden, T. E., "Windspeed and Flow Angle Measurement by Tracking of a Laser-Induced Breakdown Spark," *33rd AIAA Applied Aerodynamics Conference*, AIAA Paper 2015-2574, June 2015.

[19] Noll, R. J., "Zernike Polynomials and Atmospheric Turbulence," *Journal of the Optical Society of America*, Vol. 66, No. 3, 1976, pp. 207–211. doi:10.1364/JOSA.66.000207

[20] Gordeyev, S., and Juliano, T. J., "Optical Characterization of Nozzle-Wall Mach-6 Boundary Layers," *54th AIAA Aerospace Sciences Meeting*, AIAA Paper 2016-1586, Jan. 2016.

J. Poggie
Associate Editor